



Horus: Enhancing Safe Corners via Integrated Sensing and Communication Enabled by Reconfigurable Intelligent Surface

Qinpei Luo

luoqinpei@pku.edu.cn

Peking University

Beijing, China

Jiahao Gao

jiahao.gao@pku.edu.cn

Peking University

Beijing, China

Boya Di*

diboya@pku.edu.cn

Peking University

Beijing, China

ABSTRACT

As a key feature that has the potential to enable many advanced applications, the integration of sensing functionality is considered essential in the 6G network, which motivates the design of *integrated sensing and communication* (ISAC) systems. However, traditional ISAC systems based on non-overlapped resource allocation face the challenge of poor energy and spectral efficiency. In this paper, we implement an ISAC system named *Horus* based on reconfigurable intelligent surfaces, which provides an energy-efficient solution to sense objects in a wide range of blind areas. With a carefully designed ISAC protocol, *Horus* can transmit sensing information to the receiver with high spectral efficiency. We have verified the ability of the proposed system in two case studies of multi-modal sensing and around-corner radar early warning, respectively. Our demonstration video can be found in [11].

CCS CONCEPTS

- Human-centered computing → Ubiquitous and mobile computing systems and tools;

KEYWORDS

Reconfigurable Intelligent Surface, Integrated Sensing and Communication, Frequency Shift Keying

ACM Reference Format:

Qinpei Luo, Jiahao Gao, and Boya Di. 2024. Horus: Enhancing Safe Corners via Integrated Sensing and Communication Enabled by Reconfigurable Intelligent Surface. In *The 30th Annual International Conference on Mobile Computing and Networking (ACM MobiCom '24)*, November 18–22, 2024, Washington D.C., DC, USA. ACM, New York, NY, USA, 6 pages. <https://doi.org/10.1145/3636534.3698224>

1 INTRODUCTION

Emerging applications like autonomous driving [20], extended reality (XR) [12] and internet of things (IoT), have urged more advanced and powerful functions in the future-6G wireless networks. The ability to sense in 6G is considered essential as it provides a new paradigm to interact with the environment [6]. However, integrating

*Corresponding author

Permission to make digital or hard copies of all or part of this work for personal or classroom use is granted without fee provided that copies are not made or distributed for profit or commercial advantage and that copies bear this notice and the full citation on the first page. Copyrights for components of this work owned by others than the author(s) must be honored. Abstracting with credit is permitted. To copy otherwise, or republish, to post on servers or to redistribute to lists, requires prior specific permission and/or a fee. Request permissions from permissions@acm.org.

ACM MobiCom '24, November 18–22, 2024, Washington D.C., DC, USA

© 2024 Copyright held by the owner/author(s). Publication rights licensed to ACM.

ACM ISBN 979-8-4007-0489-5/24/11...\$15.00

<https://doi.org/10.1145/3636534.3698224>

sensing functions in mobile networks faces two challenges. First, it may require introducing complex devices to fulfill the sensing requirement, which may bring extra costs for the deployment of future 6G networks. Second, it may consume spectrum resources to realize precise sensing, leading to the degradation of the transmission data rate. To tackle the above issues, integrated sensing and communication (ISAC) emerges as a promising solution, which aims to unify the functions of sensing and communication to boost their performance mutually with high efficiency [9].

In the literature, typical ISAC approaches allocate sensing and communication sources in an orthogonal way by multiplexing to avoid interference. In [8], the author leverages the preamble of IEEE 802.11ad for sensing, thus proposing an ISAC solution in a time-division way. In [1], the author studies ISAC based on OFDM by optimizing the power allocated to each subcarrier to maximize the radar SNR. The spatial division introduced by the emerging MIMO technology provides new paradigms for ISAC, for example, the multi-antennas can be divided into different groups to realize inference-free sensing and communication[10].

However, though the above ISAC approaches based on multiplexing are relatively easy to implement, the spectrum and energy efficiency may not be guaranteed. The above mentioned works either require heterogeneous waveforms for different time/frequency resources [1, 8] or demand multiple radio frequency (RF) chains in a MIMO array manner[10]. To further reduce the burden of extra spectrum and energy, it is necessary to develop an ISAC system that leverages spectrum resources efficiently at a lower cost.

In this paper, we design and implement an ISAC system named *Horus*¹ by developing a reconfigurable intelligent surface (RIS) enabled multi-functional transceiver. The RIS serves as the transceiver antenna, consisting of multiple passive tunable elements that can alter the direction of reflected beams. It offers an energy-efficient solution for the spatial division to realize flexible sensing and communication by generating beams in various directions. Besides, via our carefully designed ISAC waveform and protocol, both sensing and communication functionality can leverage a fully unified waveform to save spectrum resources, maintaining the localization error as low as 0.1m with a stable transmission data rate. By conducting simulations along with two experimental case studies of multi-modal sensing and around-corner radar early warning, we verify the validity and robustness of the proposed system, which illustrate its potential to act as an intelligent roadside unit in vehicular networks. Our demonstration video can be found in [11].

¹The name is from the Egyptian myth of “The Eye of Horus”, which stands for surveillance and protection.

2 SYSTEM DESIGN

In this section, we first present an overview of the proposed RIS-enabled ISAC system of *Horus*, then illustrate the design of each component in detail.

2.1 System Overview

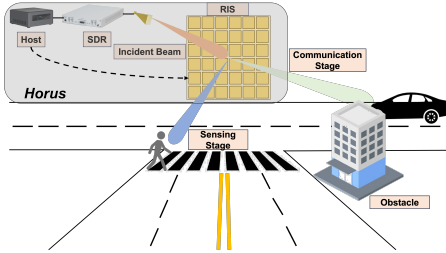


Figure 1: System Illustration of *Horus*

The whole system of *Horus* is shown in Fig. 1. We deploy a host computer to control the software-defined-radio (SDR) hardware and RIS simultaneously. The RIS is combined with horn antennas, frequency converters, and amplifiers to form the *RIS-Enabled Transmitter*, to which an SDR hardware is connected. The signals from the SDR hardware are up-converted to NR 5G mmWave band and amplified before being emitted by the horn antenna as the incident beam towards RIS, while the host controls the directions of the reflected beam by the RIS configuration.

The workflow of *Horus* can be described as follows. First, we generate the baseband signals following the designed ISAC protocol in Sec. 2.4. Second, the generated signals are processed and transmitted to the *RIS-Enabled Transmitter* by the SDR hardware. Third, depending on the specific scenario, the host can configure the RIS to direct the beam toward any object for sensing or any receiver for communication. Note that via the designed ISAC protocol, the signals for sensing and communication are identical and they can be processed by corresponding schemes, respectively. Thus we can lower the cost and improve the spectral efficiency of the integrated system.

2.2 RIS-Enabled Transmitter

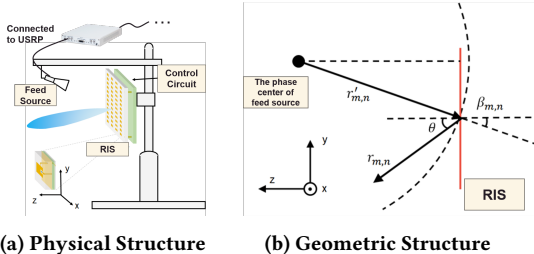


Figure 2: Illustration of RIS-Enabled Transmitter

The foundation of *Horus* is an mmWave *RIS-enabled transmitter*, providing a cost-efficient solution compared to the traditional phased array based transmitter. As shown in Fig. 2a, the feed source,

i.e., a horn antenna, is mounted above RIS and connected to the RF chain. Signals generated by the host computer are transmitted to the feed source after being processed by the USRP, which then transmits incident electromagnetic (EM) waves to the metasurface. According to Fig. 2b, we assume that RIS is on the Y-Z plane, centered by $(0, y_f, z_f)$. The horn antenna can be considered as a point source and emits EM waves on RIS in the form of spherical waves [18]. For the unit (m, n) , the electric field strength of the incident wave can be expressed by

$$E_{m,n}^{in} = \sqrt{\frac{P_{in}}{4\pi(r'_{m,n})^2} \cdot G_{m,n} \cdot S \cdot \beta_{m,n} \cdot \exp(-jk_0r'_{m,n})}, \quad (1)$$

in which P_{in} refers to the power of incident wave, $G_{m,n}$ refers to the directional coefficient of the unit (m, n) , and S denotes the area of RIS. We let θ and ϕ represent the elevation and azimuth angle in the spherical coordinate system in the reference of the center of RIS, then the electric field strength of the unit in the far-field direction (θ, ϕ) is given by

$$E_{m,n}(\theta, \phi) = E_{m,n}^{in} \sqrt{|\tau_{m,n}|^2 \frac{1}{2\pi(r_{m,n})^2} \exp(-jk_0r_{m,n}) \exp(j\arg(\tau_{m,n}))}, \quad (2)$$

where $\tau_{m,n}$ represents the reflection coefficient of the unit. To maximize the radiation intensity of the metasurface in a given beam direction, ideally, the reflection phase of each unit is given by

$$\arg(\tau_{m,n}) = k_0r'_{m,n} - k_0r_{m,n} \quad (3)$$

The phase shift of each unit is tuned discretely with 1-bit control. Each unit on the array reflects the incident waves and applies corresponding amplitude and phase changes. The control circuit communicates with the host and alters its output, thereby applying different bias voltages to each unit to configure RIS. The reflected waves from each unit can then be superimposed in a given direction, achieving beamforming functionality. The proposed *RIS-Enabled Transmitter* is designed to meet the requirements in the Table 1.

Requirements	Parameters
Operating Frequency	25-27GHz
Number of Units	32*32
Gain	22dBi
Maximum azimuth angle of beam scan	$\pm 60deg$
Maximum elevation angle of beam scan	$\pm 10deg$
Polarization Mode	Linear

Table 1: Requirements of RIS-Enabled Transmitter in *Horus*

2.3 Methodology of Sensing and Communication

2.3.1 FSK Sensing. To detect and track objects with RF, sensing systems leverage transmitted and received RF signals to get the information of range and velocity. Frequency shift keying, in the context of sensing, involves changing the frequency of the transmitted signal and comparing it with the received signal to measure the time-of-flight, which is acquired by the phase of signals. Via the host computer and USRP, we generate two sub-carriers with frequency of $f_{c,1}$ and $f_{c,2}$, transmitted signals can be expressed by

$$S_{tx,i} = A_{tx} e^{j(2\pi f_{c,i} t + \Phi)}, i = 1, 2, \quad (4)$$

where A_{tx} represents the gain at the transmitting antenna, Φ is the initial phase the phase lock loop (PLL) introduces. As the distance between the transmitting antenna and RIS can be omitted compared to the object's range, the signal's flight distance can be directly approximated by $2R$. Then the received signals can be expressed by

$$S_{rx,i} = A_{rx} e^{j(2\pi f_{c,i} t + \Phi - \frac{4\pi f_{c,i} R}{c})}, i = 1, 2, \quad (5)$$

in which A_{rx} denotes the gain at the receiving antenna. Note that in the system the transmitter and receiver share the same clock source, thus the phase introduced by PLL is the same. Thus, by multiplying the received signals with the conjugate of the transmitting antenna, we can get two phase differences as

$$S_{IF,i} = A_{rx} A_{tx} e^{-j \frac{4\pi f_{c,i} R}{c}} = A_{rx} A_{tx} e^{j\psi_i}, \psi_i = -\frac{4\pi f_{c,i} R}{c}, i = 1, 2, \quad (6)$$

from which we can derive the range of the object as

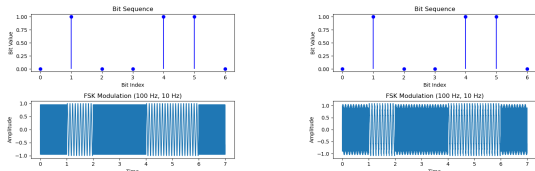
$$R = \frac{c(\psi_2 - \psi_1)}{4\pi(f_{c1} - f_{c2})}. \quad (7)$$

As we use two continuous waves in FSK, we can directly use the Doppler Effect to estimate the velocity. According to [2], if we assume the transmitting frequency is f_0 , the relationship between Doppler frequency f_D and velocity v can be depicted by

$$f_D = \frac{2f_0 v}{c}. \quad (8)$$

By analyzing f_D we can get the velocity as $v = \frac{c f_D}{2 f_0}$.

2.3.2 FSK Modulation and Demodulation. As shown above, we illustrate that the phase of FSK signals can be used for sensing to get the range and velocity of the object. Besides, the amplitude of FSK signals can be leveraged to carry information transmitted. As shown in Fig. 3a, traditional FSK modulation encodes and transmits the information by periodically shifting the frequency of the carrier, using different frequencies to represent different bit symbols.



(a) Traditional FSK Modulation (b) FSK Modulation for ISAC

Figure 3: Comparison of two methods for modulation

2.4 ISAC Protocol Design

2.4.1 Waveform designed for ISAC. In Section 2.3, we illustrate that the phase and amplitude of FSK signals can be leveraged for sensing and communication, respectively. We aim to combine them to design the waveform that can be used for ISAC to save the spectrum resource. Thus, we choose to simultaneously transmit signals

with two frequencies but with different amplitudes to encode the information as shown in Fig. 3b. For instance, when bit "1" is transmitted, the amplitude of the frequency component of $f_{c,1}$ is set to be 1 and the amplitude of the other component is 0.1, while for bit "0" is vice versa. When the aggregate signal is transmitted, the receiver for sensing is still able to identify the phase difference to sense the object, while the receiver can just follow the basic FSK demodulation scheme to get the information transmitted from *Horus*. The designed ISAC signals can also be intuitively depicted by the waterfall plot as Fig. 4.

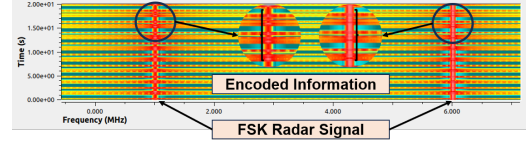


Figure 4: Waterfall plot of the ISAC signals

A challenge that needs to be addressed is that in the aggregate signal, different frequency components may experience different paths, resulting in different levels of fading, i.e., frequency selective fading, which may increase the bit error rate (BER) in *Horus* as the frequency component with higher relative amplitude may suffer from greater fading. This characteristic can be depicted by coherence bandwidth, which is defined by the frequency interval where the multipath channel experiences flat fading. Typically, the coherence bandwidth increases with the frequency. According to the measurement in [7], the coherence bandwidth of 11.2 GHz and 62.4 GHz at the 0.7 correlation level is 18.3 MHz and 32.8 MHz, respectively. As we adopt a center frequency of 26 GHz and frequency spacing of 6 MHz in *Horus*, we can ensure that the fading experienced by signals of two frequencies in the air is almost identical, which does not affect the BER of communication.

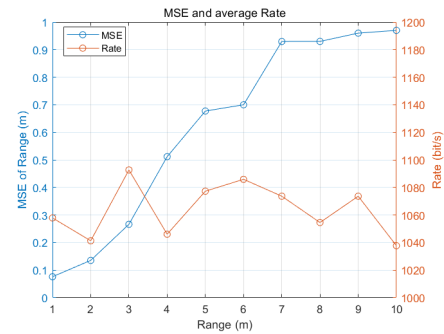


Figure 5: Mean square error and average rate against range

To estimate the proposed protocol's sensing and communication performance, we use *Gnuradio* to do the simulation. As shown in Fig. 5, we manually change the range of the object meanwhile monitoring the mean square error (MSE) of the range and average rate. The result illustrates that first, the localization MSE increases with the range while remaining under 1.0; Second, although the communication rate fluctuates continuously with the growing range,

it remains around the level of 1070 bit/s. Thus, the robustness of the designed ISAC protocol is verified concerning both sensing and communication.

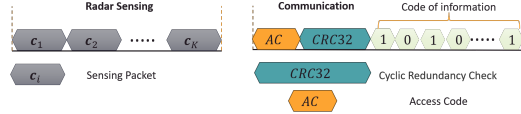


Figure 6: Frame Structure of Horus

2.4.2 Frame Structure. Fig. 6 illustrates the frame structure of the proposed system for sensing and communication. In each stage of sensing, i.e., when the host configures RIS to direct the beam toward the area that needs to be detected, the host generates K sensing packets. Each sensing packet consists of a fixed number of sampling points of the FSK signals. Once the host receives the echo signals from the object, it multiplies them with the conjugate of transmitting signals, and the result is subsequently processed by downsampling, Fast Fourier Transform, and peak detection to determine the range and velocity of the target.

The communication packet consists of three parts. We first defined a fixed bit sequence as the access code to determine the beginning of each packet. To ensure the vehicle can robustly receive and demodulate correct information from the host, we added a 32-bit cyclic redundancy check (CRC) code before encoding the information. At last, the code of transmitted information can vary depending on the specific application.

In our system, these two frames are generated simultaneously. To realize the FSK modulation proposed in the last subsection, we need to do numerical operations between two streaming sequences of sampling points from sensing and communication packets. However, to achieve sufficiently high accuracy in measuring the phase, we need to adopt a high sampling rate, under which the numerical operations between two signals may be severely affected by timing error [3]. Thus, we choose to send the communication frame with a much lower baud rate by interpolating. If the baud rate is B , and the sampling rate is f_s , then we repeat each symbol in the state information frame by $\frac{f_s}{B}$ times. In this case, even though there might be potential timing errors at the 0-1 bit transition edges, due to their small proportion in the entire sequence, the information can still be accurately transmitted.

3 IMPLEMENTATION

3.1 Horus

Fig. 7 shows the prototype of *Horus*. The host computer connects to RIS and Universal Software Radio Peripheral (USRP) via USB and Ethernet cables, respectively. The USRP model chosen is X310 [5], which has two daughterboards and independent channels, allowing simultaneous transmission and reception of signals under the same clock source. We set the center frequency of USRP to 2 GHz, to which the baseband signals generated by the host will be modulated. The TX port of one daughterboard and the RX port of the other are connected to two intermediate frequency (IF) ports of the mmWave frequency converter via two low-frequency RF cables. The frequency converter produced by TMYTEK [17] is used

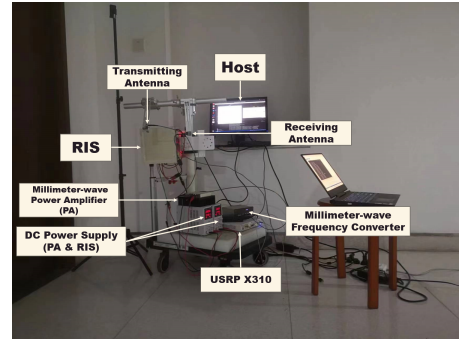


Figure 7: Prototype of Horus

to up-convert the IF signal from USRP to the 26GHz frequency band and down-convert the received high-frequency signal to the IF range. The TX port of the frequency converter is connected to the transmitting horn antenna (feed source) through an mmWave power amplifier (PA), where the SNR of the RF signal is significantly improved. The RX port of the frequency converter is connected to another horn antenna to receive the radar echo signals.

Note that both RIS and PA require DC power, thus, we use two DC power supplies with output voltages of 28V and 13.59V, respectively to power these two devices. The other devices in *Horus* are powered by the standard Chinese mains electricity, which is 220V AC.

3.2 Vehicle

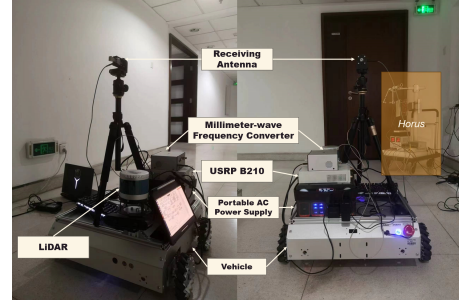


Figure 8: Prototype of Vehicle for Case Study

Fig. 8 shows the setup of the vehicle for case studies in Sec. 4. For the main body part, we directly use the product by WHEELTEC [19]. It includes a LiDAR by LSLIDAR [13]. An NVIDIA JETSON NANO [15] is deployed on the vehicle as the master computer, which not only receives and processes information from sensors but also controls the motion of the vehicle via an STM32 MCU [16]. We use an ethernet cable to connect JETSON NANO with a USRP B210 [4]. Received signals from the antenna are down-converted by the frequency converter and sent to USRP to be further demodulated by the master computer to acquire the information.



Figure 9: Horus aided multi-modal sensing

4 CASE STUDY

4.1 Multi-Modal Sensing

We first study how *Horus* can act as a supplement to the vehicle-mounted sensors. By conducting an experiment in an indoor environment, we verified the capability of *Horus* for aiding blocked sensors to achieve multi-modal sensing.

4.1.1 Experiment Setup. We first define the information transmitted under this scenario and how we encode it. To acquire the point cloud of the occluded object, we need to scan the space to get the 3D coordinates of each point. Assuming that the location of *Horus* is known to the vehicle, once the vehicle gets the range and beam angle of the point relative to *Horus*, it can determine the coordinates of the point in its own coordinate system through simple transformation. Thus, we choose to transmit the range and beam angle tuple, defined by $< r, \theta, \phi >$. Within each tuple in the communication frame, the range r is stored in the format of 32-bit float, while the azimuth and elevation angle are in the format of 32-bit int, thus, the total code length of the payload is 96 bits, i.e., 12 bytes.

Fig. 9 shows the environment setup of this scenario. We put a pile of wooden boxes beside the vehicle as an obstacle, while a chair is deployed in front of the space that *Horus* aims to detect. There are two working stages of *Horus*, the sensing stage and the communication stage. In the sensing stage, the host scans the space by changing the configuration of RIS and computing the range from radar echo signals, which are later stored in the memory with the beam angles as tuples. In the communication stage, the host configures the RIS to direct the beam toward the vehicle and transmits all the stored tuples with the frame structure for communication defined in Sec. 2.4.2.

4.1.2 Experiment Result. Fig. 9 shows the comparison between the solutions based on vehicle-mounted sensors with and without *Horus*. For a clearer illustration, the vehicle does Gaussian interpolation on the raw point cloud data from *Horus* to create a denser point cloud. It can be seen from the results that the pure vision solution based on the depth camera is severely affected because the field of view is limited by the obstacle. Besides, as the laser from LiDAR has a weak diffraction ability, it is completely blocked by the obstacle, thus the vehicle cannot sense the object behind it with a pure LiDAR solution. However, with the aid from *Horus*, the vehicle is able to sense the occluded object in a spectrum-efficient way, which offers more scalability for applications like SLAM of the home robot and intelligent roadside units in vehicular networks.



Figure 10: Scenario where Vehicle-Mounted LiDAR is limited

4.2 Around-Corner Radar Early Warning

According to [14], nearly a quarter of traffic accidents result from collisions at intersections. The obstructed view due to vehicles, buildings, and other possible sources is the main reason and accidents can occur when the vehicle-mounted sensors (LiDAR and radar) fail to perceive the blind area as shown in Fig. 10. In this subsection, we discuss how *Horus* can be leveraged as an around-corner radar. We utilize it to sense the approaching object in the blind area and communicate with the vehicle to avoid possible collision.

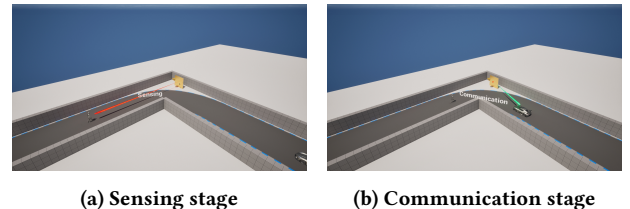


Figure 11: Horus as Around-Corner Radar

4.2.1 Experiment Setup. The scenario is shown in Figs. 11a and 11b, which includes two stages of sensing and communication. We first define a finite-state machine (FSM) with two states: **IDLE** and **ALARM**, which are carried and transmitted in the communication frame defined in Fig. 6. For more robust communication, we use two 10-bit sequences to encode the two states.

In the sensing stage, the host configures RIS to direct the beam toward the area needs to be detected and keeps recording the range

and velocity data computed from the echo signals. Assuming the initial state is **IDLE**, the whole cycle can be summarized as below:

- (1) The host first passes the raw velocity and range data points through a particle filter to smooth them and filter out outliers, which are later stored in the memory as time series.
- (2) The host set two thresholds v_{th} , n_{th} and keep monitoring the velocity. If consecutive n_{th} points with a velocity exceeding v_{th} are detected, the host determines that an approaching object is found.
- (3) If an approaching object is detected, the host use the stored time series to predict the trajectory of the object in the future several time steps.
- (4) Meanwhile, the vehicle also keeps reporting its location and speed to the host, thus, the host can estimate the trajectory of it on the same time steps as in (3).
- (5) The host checks the two trajectories from (3) and (4). If they intersect with each other, the host determines that a collision will happen. It changes the state to **ALARM** and triggers the communication stage to immediately configure the RIS to direct the beam towards the vehicle. Once the vehicle receives the information of **ALARM**, it brakes to avoid possible collision.
- (6) After the object passes the corner, the condition in (2) is no longer satisfied, *Horus* turns back to the sensing stage, change the state to **IDLE**, and starts a new cycle.



(a) The vehicle moves when no approaching object is found (b) The vehicle brakes when the approaching object is found

Figure 12: Horus as Around-Corner Radar

4.2.2 Experiment Result. In the experiment, we set the vehicle to navigate in the corridor and turn around the corner at a fixed speed, while a pedestrian is approaching the corner from the other direction. As shown in Figs. 12a and 12b, the proposed system successfully act as around-corner radar to detect the approaching object meanwhile communicating with the vehicle to avoid the collision. We also test the system's capability of communicating at the transport layer with commercial Wi-Fi devices and sockets, and the whole demo video is available at [11].

5 CONCLUSION

In this paper, we propose *Horus*, an ISAC system prototype providing an efficient solution for sensing and communication. Supported by the designed RIS-Enabled Transmitter, *Horus* is able to beam-scan a wide range of space to achieve ISAC at a relatively lower cost compared to the MIMO array. Besides, with the proposed ISAC protocol based on FSK, *Horus* can leverage the same channel for both sensing and communication to save spectrum resources. We

also utilize the proposed *Horus* in two case studies and verify its capability of providing a new sensing paradigm with communication ability, which has the potential for advanced applications such as indoor SLAM and intelligent roadside units in vehicular networks.

6 ACKNOWLEDGEMENTS

This work was supported by National Key R&D Project of China under Grant No. 2022YFB2902800; in part by the National Science Foundation under Grants 62322101, 62227809, 62271012; and in part by the Beijing Natural Science Foundation under Grants 4222005 and L212027.

REFERENCES

- [1] Marian Bică and Visa Koivunen. 2019. Radar Waveform Optimization for Target Parameter Estimation in Cooperative Radar-Communications Systems. *IEEE Trans. Aerospace Electron. Systems* 55, 5 (2019), 2314–2326. <https://doi.org/10.1109/TAES.2018.2884806>
- [2] VC. Chen, F. Li, S.-S. Ho, and H. Wechsler. 2006. Micro-Doppler effect in radar: phenomenon, model, and simulation study. *IEEE Trans. Aerospace Electron. Systems* 42, 1 (2006), 2–21. <https://doi.org/10.1109/TAES.2006.1603402>
- [3] Markus Dillinger, Kambiz Madani, and Nancy Alonistioti. 2005. *Software defined radio: Architectures, systems and functions*. John Wiley & Sons.
- [4] a National Instruments Brand Ettus Research. [n. d.]. USRP B210 USB Software Defined Radio (SDR). <https://www.ettus.com/all-products/usb210-kit/>
- [5] a National Instruments Brand Ettus Research. 2024. USRP X310 High Performance Software Defined Radio. <https://www.ettus.com/all-products/x310-kit/>
- [6] Linqing Gui, Wenyang Yuan, and Fu Xiao. 2023. CSI-based passive intrusion detection bound estimation in indoor NLoS scenario. *Fundamental Research* 3, 6 (2023), 988–996. <https://doi.org/10.1016/j.fmre.2022.05.015>
- [7] Jean-Philippe Kermoal, A. Hammoudeh, and M. Sanchez. 1998. A Comparison of Coherence Bandwidth Measurements at 11.2 and 62.4GHz for Indoor Line of Sight Microcells. In *1998 28th European Microwave Conference*, Vol. 2. 351–356. <https://doi.org/10.1109/EUMA.1998.338177>
- [8] Preeti Kumari, Junil Choi, Nuria González-Prelcic, and Robert W. Heath. 2018. IEEE 802.11ad-Based Radar: An Approach to Joint Vehicular Communication-Radar System. *IEEE Transactions on Vehicular Technology* 67, 4 (2018), 3012–3027. <https://doi.org/10.1109/TVT.2017.2774762>
- [9] Fan Liu, Yuanhao Cui, Christos Masouros, Jie Xu, Tony Xiao Han, Yonina C. Eldar, and Stefano Buzzi. 2022. Integrated Sensing and Communications: Toward Dual-Functional Wireless Networks for 6G and Beyond. *IEEE Journal on Selected Areas in Communications* 40, 6 (2022), 1728–1767. <https://doi.org/10.1109/JSCC.2022.3156632>
- [10] Fan Liu, Christos Masouros, Ang Li, Huafei Sun, and Lajos Hanzo. 2018. MU-MIMO Communications With MIMO Radar: From Co-Existence to Joint Transmission. *IEEE Transactions on Wireless Communications* 17, 4 (2018), 2755–2770. <https://doi.org/10.1109/TWC.2018.2803045>
- [11] Qinpei Luo. [n. d.]. Demo Video. https://www.youtube.com/watch?v=t3A_k3jifyo&ab_channel=QPLuo
- [12] Qinpei Luo, Hongliang Zhang, Minrui Xu, Boya Di, Anthony Chen, Shiwen Mao, Dusit Niyato, and Zhu Han. 2023. An Overview of 3GPP Standardization for Extended Reality (XR) in 5G and Beyond. *GetMobile: Mobile Comp. and Comm.* 27, 3 (nov 2023), 10–17. <https://doi.org/10.1145/3631588.3631592>
- [13] Leishen Intelligent System The most complete LiDAR manufacturer. [n. d.]. 32/16-Line Mechanical LiDAR. <https://lslidar.com/product/c32-16-mechanical-lidar/>
- [14] Wassim G Najm, John D Smith, Mikio Yanagisawa, et al. 2007. *Pre-crash scenario typology for crash avoidance research*. Technical Report. United States. Department of Transportation. National Highway Traffic Safety.
- [15] NVIDIA. [n. d.]. NVIDIA Jetson Nano. <https://www.nvidia.com/en-us/autonomous-machines/embedded-systems/jetson-nano/>
- [16] STMicroelectronics. [n. d.]. STM32 32-bit Arm Cortex MCUs. <https://www.st.com/en/microcontrollers-microprocessors/stm32-32-bit-arm-cortex-mcus.html>
- [17] TMYTEK. [n. d.]. UD Box 5G | Up/down converter, frequency converter. <https://www.tmytek.com/products/frequency-converters/udbox5g>
- [18] Xiang Wan, Mei Qing Qi, Tian Yi Chen, and Tie Jun Cui. 2016. Field-programmable beam reconfiguring based on digitally-controlled coding metasurface. *Scientific reports* 6, 1 (2016), 20663.
- [19] Wheeltac. [n. d.]. Wheeltac. <https://wheeltac.net/product/html/?174.html>
- [20] Minrui Xu, Dusit Niyato, Junlong Chen, Hongliang Zhang, Jiawen Kang, Zehui Xiong, Shiwen Mao, and Zhu Han. 2023. Generative AI-Empowered Simulation for Autonomous Driving in Vehicular Mixed Reality Metaverses. *IEEE Journal of Selected Topics in Signal Processing* 17, 5 (2023), 1064–1079. <https://doi.org/10.1109/JSTSP.2023.3293650>